Structural health monitoring of composite laminates in thermoplastic induction welded joints using electromagnetic field technique

Mattia Mazzeschi [a,b,*], Saman Farhangdoust [b], Esteban Cañibano [a], Juan C. Merino [a,c], Karina C. Núñez [a,c,*]

[a] *Foundation for Research and Development in Transport and Energy (CIDAUT), Spain*
[b] *Structures and Composites Laboratory (SACL), Aeronautics and Astronautics Department, Stanford University, USA*
[c] *Department of Condensed Matter Physics, Faculty of Sciences, University of Valladolid, Spain*

ARTICLE INFO

ABSTRACT

This research paper explores the assessment of electrical property changes resulting from damage in a Carbon Fiber Reinforced Polymers (CFRP) laminate and its thermoplastic induction-welded joints. Controlled variations in electrical conductivity and dielectric permittivity were achieved by incorporating square Polytetrafluoroethylene (PTFE) adhesive tapes into both CFRP laminates and the bondline interfaces of induction-welded components. Two elementary and effective sensors, capable of measuring magnetic (Purely Magnetic sensor) and electric fields (Hybrid sensor), were employed to detect these property changes induced by a sinusoidal magnetic field generated by a nearby coil. Both sensors exhibited remarkable sensitivity in identifying variations induced by the smallest artificial defects, measuring 2×2 mm in size. Furthermore, the PM sensor displayed a discernible signal trend corresponding to changes in defect size ranging from 4 to 225 mm square, as well as variations in position within the thickness of the CFRP laminate, extending to a depth of 1.7 mm. These findings underscore the potential of electromagnetic-based structural health monitoring (ESHM) techniques for monitoring the condition of a thermoplastic composite structure and its induction-welded joints.

1. Introduction

Thermoplastic composites (TPCs) offer promising alternatives to thermoset composites in the aerospace industry, primarily due to their more cost-effective manufacturing processes and substantial environmental advantages such as reduced energy requirements and improved recyclability [1]. The thermoplastic composite market in the aerospace and defense industry is projected to grow at a *compound annual growth rate* (CAGR) of 6.26 % from 2022 to 2030, reflecting the increasing industry interest in this material [2].

Several aircraft incorporate TPCs in both structural and non-structural components. For example, Airbus has employed thermoplastic skins, panels and leading edges in A340–600 and A380 aircrafts. Additionally, brackets and fuselage clips in Airbus 350 XWB, as well, as passenger door beams and angled profiles in the Boeing 787, highlight the growing importance of TPCs in various aerospace applications.

The distinctive feature of thermoplastic matrices, which can be melted repetitively with nominal loss of physical properties, enables the implementation of fusion bonding techniques, potentially resulting in weight saving though the elimination of aircraft fasteners and adhesives. Moreover, one of the primary factors contributing to the cost-effectiveness of TPCs is the ability to overcome typical issues associated with conventional joining processes, such as stress concentrations and delaminations due to hole drilling, as well as lengthy surface preparation and curing cycles required for adhesive bonding. Fusion bonding processes involve heating and subsequently cooling the polymer at the interface of two components to achieve consolidation [3]. The specific method used depends on how the necessary heat for melting the joint interface is applied. Among the various techniques, ultrasonic [4, 5] resistance [6,7] and induction welding [8–10] are considered to be most suitable for thermoplastic. Induction welding relies on the generation of eddy currents within the material by the coil, which leads to the conversion of electrical energy into heat.

This method has gained prominence within the past two decades and is increasingly recognized as a highly efficient approach for rapidly processing fiber-reinforced thermoplastic composites [8], [9]. Induction

---

welding potentially allows for geometrically complex welds and does not require any contact with the welding stack for heating, increasing flexibility and simplifying automation [11]. Gulfstream G650 was the first commercial airplane to use induction welding for critical control surfaces, specifically rudders and elevators. Rapid, efficient and flexible thermoplastic welding operations could also benefit the emerging field of the urban air mobility (UAM), where high-volume and high-quality production are crucial. Despite these advantages, TPCs are not immune to damages, such as cracks and delamination caused by fluctuating or impact stresses. Unlike metals, predicting the progression of damage in composite structures [12] remains challenging, making it difficult to estimate regular inspection intervals. This poses a challenge to the current maintenance approach, especially in the context of a future scenario characterized by numerous airline fleets and high volume electric Vertical Take-Off and Landing (eVTOLs). This situation has led to the need for a change towards condition-based maintenance (CBM) wherein maintenance is only undertaken when specific indicators reveal decreasing performance or an impending failure [13], [14]. Structural health monitoring (SHM) could facilitate a comprehensive understanding of the damage progression by integrating sensors into the monitored structure, collecting, and analyzing the generated data over the service life to identify the presence, location, and type of damage. The successful implementation of CBM paradigm hinges on the capability of SHM systems to assess the component's state of health during flight or in preflight checks.

SHM field is characterized by a wide range sensing techniques for detecting in-service damages in aerospace composite structures, such as guided waves [15–17], acoustic emissions [18–20], methods based on fiber optic sensors [21,22], phased array ultrasonic [23,24], vibration methods [25–27], impedance (EMI)[28] and electrical impedance tomography [29,30]. Electromagnetic-based SHM (ESHM) techniques operate that the presence of damage locally affects the electromagnetic characteristics of the material, specifically the electrical conductivity and/ or the dielectric permittivity in the case of fibers reinforced polymers. Damage resulting from mechanical factors, such as delamination or fiber breakages, locally impacts the electrical conductivity of the material. Conversely, contamination, such as liquid ingress, which can lead to a loss of mechanical performance in TPCs due to the chemical reactions, primarily changes the dielectric permittivity of the medium. Mazzeschi et al. have provided a summary table detailing how defects of different origins influence electrical properties [31]. One of the most relevant aspects of ESHM is that designing the sensitive system appropriately to assess both electrical conductivity and/or dielectric permittivity and constructing a correlation between these properties and the type of inspected defect, it is possible to gain access to many kinds of damage occurring in aircraft structures. Moreover, ESHM techniques provide the potential to detect defects that might not be readily visible with more established SHM methods. As an instance, the pyrolysis of the resin caused by electrical impacts (e.g., sparks, lightning) that do not induce any delamination, cannot be detected using ultrasonic guided waves (UGW) (28). In fact, the change in the propagation medium for mechanical waves is minimal, while pyrolysis of the resin induces an appreciable change in electrical permittivity, detectable by ESHM techniques.

The influence of temperature variation in UGW damage detection and localization remains a challenge [32]. Temperature fluctuation affects the speed, amplitude, phase of ultrasonic waves [33] and also the material properties of the piezoelectric transducer. Different temperature compensation techniques exist but at the expense of high computational cost and reference to pristine values which are not readily available [34]. ESHM techniques, on the other hand, are often employed in high temperature environment (e.g. Conductivity measurement of heat treated aluminum components to check hardness and tensile strength [35]. Different temperature compensation techniques have been developed and validated for operating condition with rapid temperature changes.[36–39].

Although ESHM techniques, in particular eddy currents-based method, are typically used for conductive materials such as metals, they have found applications in composite materials despite their low conductivity. These methods exhibit good sensitivity to the conductivity changes associated with alternations in fibers positions, directions, or fiber cracking are demonstrated in [40]. Liu et al. [41] shows the capability of their eddy current array sensing film to monitor damage around the hole-edge of composite bolted joint. Different ESHM approaches have been successfully implemented for damage diagnostic imaging [42–44]. Recent advancements in electrical resistance-based SHM techniques by Zhang et. al [45–48] have demonstrated the efficacy of high-stability MXene [47,48] and buckypaper sensors [45,46]. These sensors have shown exceptional sensitivity and stability in monitoring mechanical behavior, damage evolution, and fatigue in composite structures, including bonded-riveted joints, bolted joints, and repaired wind turbine blades. However, this method monitors local variations in electrical resistance, but faults associated with variations in dielectric permittivity alone, such as the ingress of liquids (e.g., water, oil, fuel), may not be detectable. Moreover, while these prior studies predominantly concentrated on assessing signal variations associated solely with the presence of damage, there exists a necessity for a more thorough examination of the correlation between sensor response and variations in electromagnetic properties induced by defects within the composite material. The aim of the present research is to not only assess defect induced signal variation but also delve deeper into investigating the correlation between sensor response and controlled local variations in both electrical conductivity and dielectric permittivity. Moreover, the current research pioneers the application of ESHM techniques specifically for induction welded joints, marking the first instance of such application in the field.

To date, there is lack of instances in the literature where ESHM techniques have been utilized to assess induction-welded CFRP joints. Existing research primarily revolves around the monitoring of thermoplastic welded components, primarily emphasizing ultrasonic and microwave welding techniques. These studies predominantly make use of guide waves [49–51] and electrical resistance-based SHM methods to assess the integrity of the joints [52]. In a prior study by the authors [31], a numerical approach demonstrated the potential of using measurements related to the attenuation and reflection of the incident magnetic field on a CFRP welded joint as a viable strategy for assessing joint health. However, the efficacy of this method required experimental validation. Additionally, the initial research solely considered defects that influenced changes in electrical conductivity, yet variations in dielectric permittivity are equally pertinent.

The current study aims to explore the interplay between alterations in both electrical conductivity and dielectric permittivity properties due to damage in CFRTP when subjected to an exciting magnetic field. This exploration employs two distinct measurement methodologies: one based on assessing local changes in the magnetic field through a reception loop and the other focused on measuring changes in the electric field using a pair of sensing electrodes. Respect to the previous studies, the present research prioritized a simple sensor design while maintaining excellent damage sensitivity, offering benefits such as enhanced signal interpretation and streamlined modeling of sensor behaviour. This approach facilitates a clearer understanding of the correlation between sensor response and changes in electrical conductivity and dielectric permittivity properties.

2. Materials and methods

A carbon fiber reinforced thermoplastic polymer (CFRTP) structure inherently comprises two distinct media: conductive carbon fibers and dielectric resin component. Variations in the local electrical conductivity and dielectric permittivity of these materials affect the electromagnetic field generated by a specific source and subsequent eddy current induction. Regions with heightened electrical conductivity facilitate

preferential pathways for current propagation, leading to intensified field line concentration and an increase in the resultant eddy currents. Concurrently, deviations in dielectric permittivity dictate the depth of electric field penetration, resulting in consequential adjustments in electromagnetic energy distribution and, in turn, alterations in eddy current spatial-temporal dynamics.

In this study, a sinusoidal time-varying magnetic field is generated by a single-loop coil (emission loop) in close proximity to the inspected materials. The emission loop consists of a copper circular trace, 800 μm in width, fabricated using the photolithography process on a 25×14 mm FR4 epoxy glass fiber substrate. Two distinct measurement methodologies were employed to meticulously investigate the interaction between alterations in electrical properties caused by damage in CFRTP, and the exciting magnetic field. The first methodology is based on the measuring the magnetic field using a sensing loop positioned between the emission loop and the material under inspection (Fig. 1.a). The second approach involves measuring changes in the electric field caused by the presence of a defect, utilizing a pair of sensing electrodes (Fig. 1.b). Following the nomenclature provided by Lemistre [44], we will name the first method purely magnetic method (involving magnetic field excitation and detection) and the second method as the hybrid method (involving magnetic field excitation and electric field detection). The reception loop and the two electrodes are formed by 800 μm width traces, which are produced using the photolithography process on the opposite side of the FR4 epoxy glass fiber substrate respect to the emission loop.

In an initial phase, a laminate having a series of artificially generated defects reproducing local variations in electrical properties was inspected with the objective of assessing whether the two measurement techniques were able to capture these variations. The defect was generated by placing a square Polytetrafluoroethylene (PTFE) adhesive tape on a defined ply during the stacking operation (Fig. 2). PTFE adhesive tape has a relative dielectric permittivity about half of that of the resin used in the composite (Polyphenylene sulfide, PPS) and accounts for local variation in dielectric permittivity. At the same time, the presence of the PTFE tape gives rise to ply folds that inevitably affect the distribution of induced currents. At the PTFE tape, there is also a localized increase in fiber filling rate since the fibers are compressed more tightly against each other. This compression increases the contact points between the fibers, and consequently leading to a local rise in electrical conductivity. Senghor et al. [53] developed a simplified analytical model based on Hertz contact theory and Holm's formula in order to define the electrical resistance R_f between fibers in contact and obtained the following formula:

$$R_f = \frac{\rho}{\sqrt[3]{\left(\frac{3rF_c}{E}\right)}} \#$$ (1)

where ρ, E, r are respectively the intrinsic resistivity, elastic modulus and the radius of carbon fibers and F_c is the applied local load between neighbouring fibers. As the filing rate increases, similarly, the local forces and contact areas between neighboring fibers also increase, resulting in a consequent reduction in electrical resistance, as expressed by the equation. Defects of different sizes, localized at different ply positions along the thickness, were generated, as shown below in the section on test specimens and manufacturing.
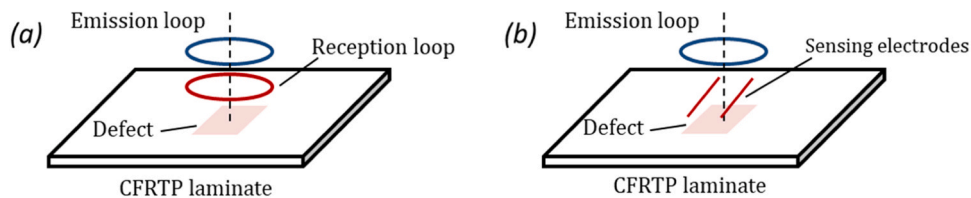
In the second step, after evaluating the damage detection capability of the two employed methods for a single laminate, measurements are conducted on thermoplastic welded lap joints. The close presence of the edges of the joint produces a distortion of the magnetic field lines generated by the emission loop and consequently the eddy currents themselves are distorted, potentially affecting the damage sensitivity of the sensors used as shown in Fig. 3.

The deliberate choice to attach the sensors to the surface of the material instead of embedding them within it minimizes potential interference with the mechanical properties of the components under investigation, thus ensuring a non-invasive approach. By avoiding the integration of sensors into the material, we reduce the risk of altering its properties or introducing structural weaknesses [54,55]. Furthermore, electromagnetic sensors are engineered to interact with electromagnetic fields, which can penetrate materials to varying depths depending on their properties, due to their operational principle. This inherent characteristic makes electromagnetic sensors well-suited for non-invasive or surface-mounted applications [56].

2.1. Theoretical consideration

In classical electromagnetism, the behaviour of electric and magnetic fields, as well as their interactions with charges and currents, is described by Maxwell's equations. The equations can be formulated in differential form or integral form. The differential form leads to the following partial differential equations (PDEs) expressed by:

$$\nabla \times \boldsymbol{H} = \boldsymbol{J}_f + \frac{\partial \boldsymbol{D}}{\partial t} \quad (Maxwell-Amp\grave{e}re's\,law)\#$$ (2)

$$\nabla \times \boldsymbol{E} = -\frac{\partial \boldsymbol{B}}{\partial t} \quad (Faraday's\,law)\#$$ (3)

$$\nabla \bullet \boldsymbol{D} = \rho_f \quad (Gauss'law - electric\,form)$$ (4)

$$\nabla \bullet \boldsymbol{B} = 0 \quad (Gauss'law - magnetic\,form)$$ (5)

where $\boldsymbol{H}$ and $\boldsymbol{E}$ are respectively the electric and magnetic field intensity, $\boldsymbol{B}$ and $\boldsymbol{D}$ respectively the magnetic and electric flux density, ρ_f and $\boldsymbol{J}_f$ respectively the electric charge density and the current density associated to the free charges. The constitutive equation relations describe the relation between the field $\boldsymbol{E}$, $\boldsymbol{B}$, $\boldsymbol{D}$ and $\boldsymbol{H}$ and could be expressed in most materials as

$$\boldsymbol{D} = \varepsilon_0 \boldsymbol{E} + \boldsymbol{P} \#$$ (6)

$$\boldsymbol{B} = \mu_0 (\boldsymbol{H} + \boldsymbol{M}) \#$$ (7)

$\boldsymbol{P}$ is the electric polarization vector describing how the material is polarized when an electric field E is present. The magnetization vector $\boldsymbol{M}$ describes how the material is magnetized when a magnetic field $\boldsymbol{H}$ is present. ε_0 and μ_0 are respectively the dielectric permittivity and the magnetic permeability of the vacuum.

For linear materials, the polarization is directly proportional to the electric field ($\boldsymbol{P} = \varepsilon_0 \chi_e \boldsymbol{E}$, where χ_e is the electric susceptibility) and the magnetisation is directly proportional to the magnetic field ($\boldsymbol{M} = \chi_m \boldsymbol{H}$, where χ_m is the magnetic susceptibility). Many CFRP laminates are anisotropic and χ_e and χ_m has to be considered tensors, both dependent

Fig. 1. Schematic representation of (a) purely magnetic and (b) hybrid method.
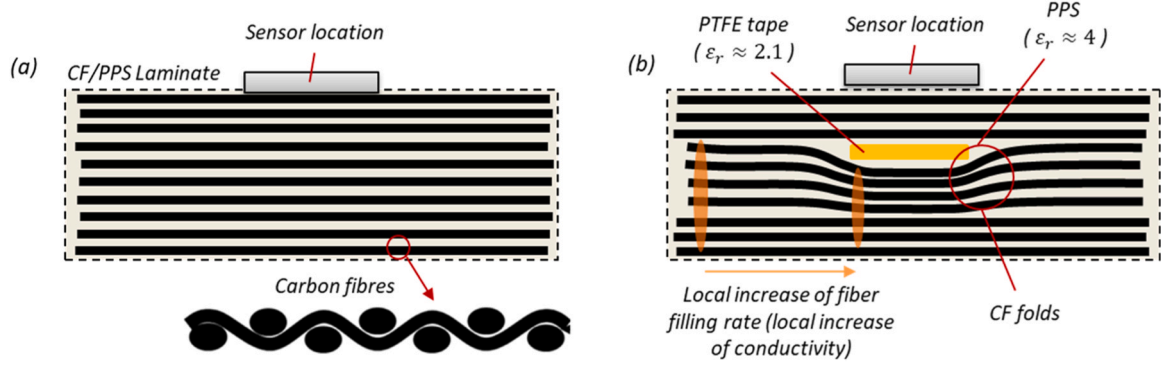
Fig. 2. Schematic representation of (a) pristine CFRP laminate and (b) laminate with embedded PTFE adhesive tape producing a local change of electrical conductivity and dielectric permittivity.
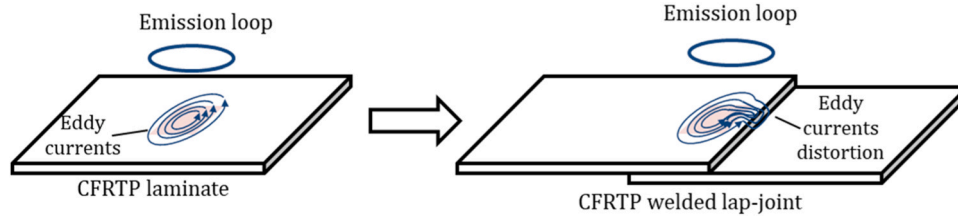

Fig. 3. Eddy current distortion due to the edge effects when transitioning from inspecting a CFRTP laminate to a CFRTP welded lap joint.

on the frequency of excitation.

In the research, low-frequency excitation was considered, specifically between 1 kHz and 7 MHz. Within this frequency range, a number of simplifications are feasible:

- The response of the polymeric resin to an applied electric field can be approximated as quasi-static: At the microscopic level, dielectrics consist of basic electric dipoles arranged randomly in space. When a dielectric substance is subjected to an electric field, these fundamental dipoles tend to align themselves with the direction of the applied electric field. As a consequence, the reaction of a solid dielectric to an externally applied electric field will be significantly influenced by the frequency of the field and the dielectric permittivity is often treated as a complex function of the frequency of the applied field. Nevertheless, when dealing with low-frequency stimulation, it becomes plausible to assume that dipoles promptly align in response to the impacting electric field and permittivity frequency dependence could be neglected. In this study, the matrix employed is PPS, characterized by dielectric strength typically ranging from 22 to 28 kV/mm, and dielectric constant, which falls around 4.0 [57].
- Negligible magnetic response of carbon fibers: When exposed to a high-frequency alternating electromagnetic wave, where the skin depth exceeds the diameter of the fibers, carbon-fiber composites demonstrate a pronounced and robust dynamic diamagnetic response (GHz bandwidth) [58]. In contrast for low excitation frequency, carbon fibers present weak diamagnetic response. Subsequently, we can consider an almost negligible magnetic susceptibility, leading to the derivation of the subsequent equation $\boldsymbol{B} = \mu_0\boldsymbol{H}$.

An equivalent form of the Gauss law where electric field intensity E appears, can be obtained by substituting the equation [6] in [4]:

$$\nabla \bullet \boldsymbol{E} = \frac{\rho_f + \rho_p}{\varepsilon_0} \#$$ (8)

where $\rho_p = -\nabla \bullet \boldsymbol{P}$ is the apparent density of the charges due to the polarization phenomenon. So, the electric field can be considered as a

resultant of two components, the field resulting from the free charges $\boldsymbol{E_f}$ ($\nabla \bullet \boldsymbol{E_f} = \rho_f/\varepsilon_0$) and the field resulting from the polarization phenomenon $\boldsymbol{E_p}$:

$$\boldsymbol{E} = \boldsymbol{E_f} + \frac{\boldsymbol{P}}{\varepsilon_0} \#$$ (9)

Considering the ohm law $\boldsymbol{J_f} = \sigma\boldsymbol{E_f}$, the relation $\boldsymbol{P} = \varepsilon_0\chi_e\boldsymbol{E_{applied}}$ and the relation $\varepsilon_r = 1 + \chi_e$, the following relation is obtained:

$$\boldsymbol{E_m} = \frac{\boldsymbol{J_c}}{\sigma} + (\varepsilon_r - 1)\boldsymbol{E_{applied}} \#$$ (10)

So, the measured electric field $\boldsymbol{E_m}$ is a function of the conductivity σ of the medium and also of its relative dielectric permittivity ε_r. These theoretical considerations play a crucial role in presenting the operational concept of the sensors utilized in this investigation.

2.2. Working principle of EM sensors

In Fig. 4, the employed sensors are schematically depicted. The purely magnetic sensor (PM) is comprised of two concentric loops: an excitation loop accountable for generating a time-varying magnetic field and a pick-up loop designed to quantify the magnetic field. On the other hand, the hybrid sensor (H) utilizes an identical magnetic excitation to the PM configuration, yet it integrates two sensing electrodes for the assessment of alterations in the electric field.

3. PM sensor working principle

For the purely magnetic method, Faraday's law (Eq. 3) comprehensively describes the interactions between emission loops, reception loops and CFRTP laminate. When an alternating current is applied to energize the emission loop, a time-varying magnetic field is generated. The voltage induced in the reception loop is directly proportional to the rate of change of the magnetic induction flux density over time:

$$V_{induced,loop} = \oint_{\partial\Sigma} \boldsymbol{E} \bullet \boldsymbol{dl} = -\int_{\Sigma} \frac{\partial\boldsymbol{B}}{\partial t} \bullet \boldsymbol{dS} \#$$ (11)
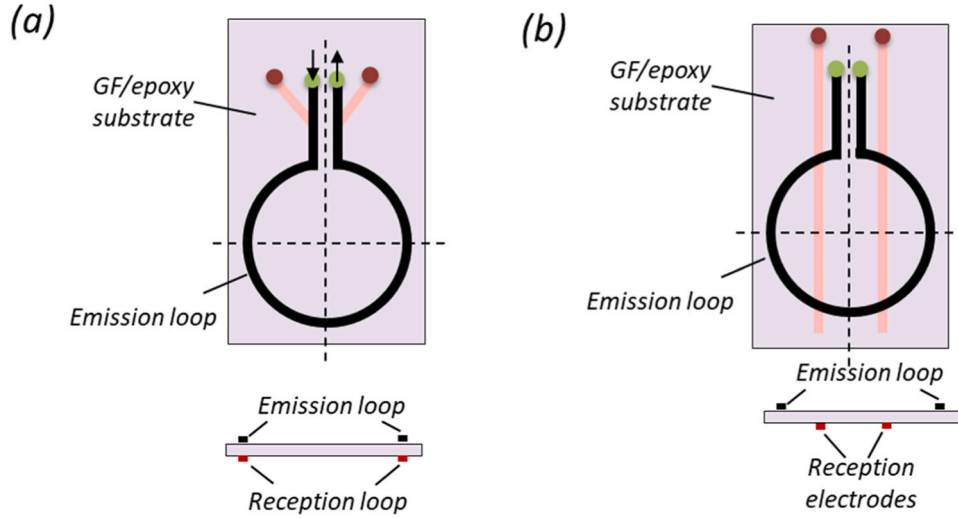
Fig. 4. Schematic representation of (a) purely magnetic (PM) and (b) hybrid (H) sensor.

where, as indicated in the figure, Σ is a surface bounded by the closed contour $\partial\Sigma$, $\boldsymbol{dl}$ is an infinitesimal vector element of the contour $\partial\Sigma$, and dS is an infinitesimal vector element of surface Σ. If the surface Σ **is not changing in time**, the equation [11] can be rewritten:

$$V_{induced,loop} = \oint_{\partial\Sigma} \boldsymbol{E} \bullet \boldsymbol{dl} = -\frac{d}{dt}\int_{\Sigma} \boldsymbol{B} \bullet \boldsymbol{dS} \# \tag{12}$$

The surface integral is the explicit expression for the magnetic flux $\boldsymbol{\Phi_B}$ through Σ. For time-harmonic systems:

$$V_{induced,loop} = -j\omega\Phi_{ij}(\boldsymbol{B}) \# \tag{13}$$

When the emission loop approaches an electrically the CFRTP laminate, the primary alternating magnetic field penetrates the material and generates continuous and circular eddy currents. The induced currents flowing within the test piece generate a secondary magnetic field that tends to oppose the primary magnetic field. An analytical model describing the interaction between PM sensor and the CFRTP laminate can be employed to establish the relationships between the sensor signal and the target properties. The model is based on a transformer representation, as shown in Fig. 5. The primary circuit represents the emission loop. The other two circuits represent the reception loop and the CFRTP laminate. R_0 and L_0 is the resistance and inductance of the emission loop; R_1 and L_0 is the resistance and inductance of the reception loop; R_e and L_e is the resistance and inductance of the induced eddy current loop in CFRPT laminate, respectively; M_{01}, M_{0e} and M_{1e} represent the mutual inductances describing respectively the interactions between emission loop-reception loop, emission loop-CFRTP laminate and reception loop-CFRTP laminate.

For the general case where the reception loop is closed (Fig. 5.a), the governing equations are:

$$\begin{cases} V_g = R_0 I_C + j\omega L_0 I_C - j\omega M_{01} I_1 - j\omega M_{0e} I_e \#\#\#\#\# \\ \quad 0 = R_1 I_1 + j\omega L_1 I_1 - j\omega M_{01} I_C - j\omega M_{1e} I_e \# \qquad \# \\ \quad 0 = R_e I_e + j\omega L_e I_e - j\omega M_{0e} I_C - j\omega M_{1e} I_1 \# \end{cases} \tag{14}$$

Where $\omega = 2\pi f$ and f is the excitation of the emission loop. Nevertheless, in the current application, the reception loop serves the purpose of detecting the magnetic field, and our focus lies in minimizing its interaction with the emission loop and CFRTP plate. Thus, the reception loop operates in an open mode, gauging the voltage at its endpoints. The governing equations then become:

$$\begin{cases} V_g = (R_0 + j\omega L_0) I_C - j\omega M_{0e} I_e \\ \quad V_1 = -j\omega M_{10} I_C - j\omega M_{1e} I_e \qquad \# \\ \quad 0 = (R_e + j\omega L_e) I_e - j\omega M_{0e} I_C \end{cases} \tag{15}$$

By making the current I_e explicit in the third equation of [15] and substituting it into the remaining two equations, the following solution can be obtained:

$$V_g = (R_C + j\omega L_C) I_C \# \tag{16}$$

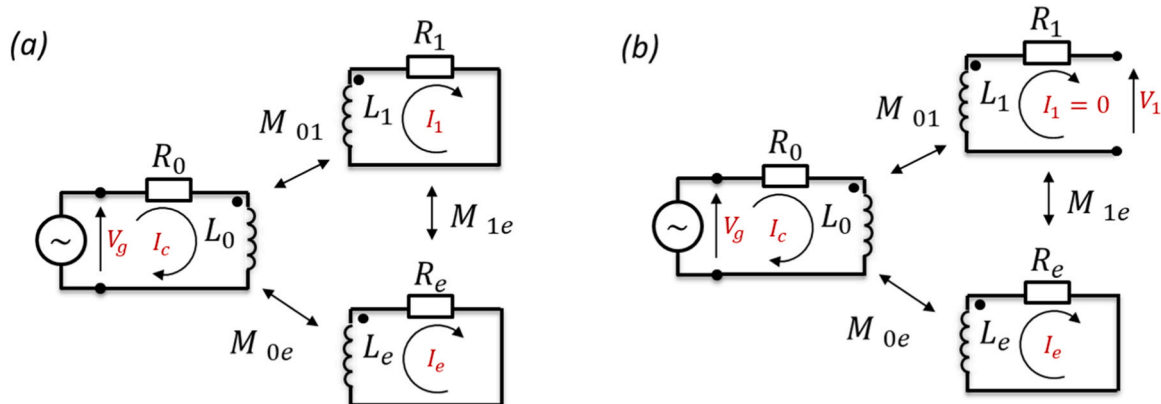$$V_1 = (R_S - j\omega L_S) I_C \# \tag{17}$$

Fig. 5. Model of emission, reception loops and CFRTP laminate interaction based on a transformer for two different cases: (a) closed and (b) open reception loop.

Where R_C and L_C is respectively the equivalent resistance and inductance of the emission loop and R_S and L_S the equivalent resistance and inductance of the reception loop:

$$R_C = R_0 + \frac{\omega^2 M_{0e}{}^2}{R_e{}^2 + (\omega L_e)^2}R_e \#\tag{18}$$

$$L_C = L_0 - \frac{\omega^2 M_{0e}{}^2}{R_e{}^2 + (\omega L_e)^2}L_e \#\tag{19}$$

$$R_S = \frac{\omega^2 M_{0e}M_{1e}}{R_e{}^2 + (\omega L_e)^2}R_e \#\tag{20}$$

$$L_S = -M_{10} + \frac{\omega^2 M_{0e}M_{1e}}{R_e{}^2 + (\omega L_e)^2}L_e \#\tag{21}$$

In instances where the PM sensor is unattached or positioned at a significant distance from the CFRPT plate, the plate's interaction is absent, resulting in both M_{0e} and M_{1e} becoming negligible. This state will be referred to as the "on air" response of the PM sensor. In this case, the emission loop is characterized by the parameters R_0 and L_0. The reception loop is defined by just the mutual inductance M_{10} and consequently, the voltage within the reception loop is expressed as follows:

$$V_1 = -j\omega M_{10}I_C \#\tag{22}$$

When a conductive test piece is approached, the complex impedance of the emission and reception loop are characterized by additional terms expressing the effect of the induced currents in CFRTP laminate. The existence of defect affects the coupling between the emission loop, reception loop and the eddy current loop, which is indicated by mutual inductances M_{0e} and M_{1e}. As shown in Fig. 2, the inclusion of integrated PTFE tape within the laminate induces alterations in the paths of eddy currents. This modification varies according to the dimensions and location of the PTFE tape across laminate thickness.

4. H sensor working principle

For H sensor configuration, the interaction between the emission loop and the CFRTP plate is effectively elucidated by the equations previously presented, particularly equations [16,18], and [19]. The distinction lies in the nature of the measurement: while the PM sensor entails magnetic field measurement, the H sensor involves an electric field assessment using two sensing electrodes. As outlined in equation [10], alterations in local electrical conductivity and dielectric permittivity, induced by defects within the laminate, manifest as corresponding modifications in the electric field concerning the initial pristine state of the material as schematically shown in Fig. 6. In accordance with Faraday's law, the time-variant magnetic field produced by the loop induces a varying electric potential along the length of the electrode.
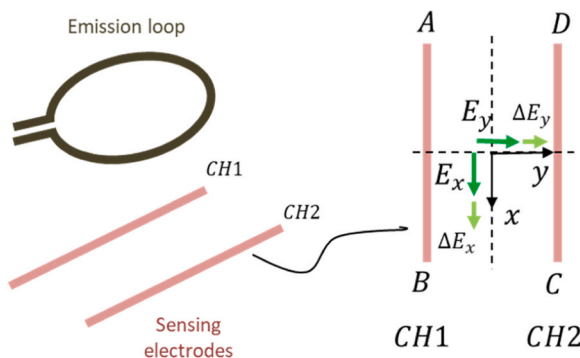

Fig. 6. Schematic H sensor representation highlighting the change of electric field components due to defect presence.

Each electrode within the system serves to convert the detected electric field into electrical signals which is voltage signal in the present study.

Furthermore, the close proximity of the two sensing electrodes gives rise to a capacitive coupling effect, leading to the accumulation of electric charge on the electrode surfaces due to their inherent capacitance. This capacitive effect exhibits a frequency-dependent behaviour, with its prominence intensifying at higher frequencies. Within the scope of our current research, we conduct a differential measurement between the two electrodes. By measuring the voltage difference between the two electrodes, common-mode noise and interference can be cancelled out, enhancing the accuracy of the electric field measurement. In the context of this differential measurement utilizing two sensing electrodes, our focus is specifically directed towards quantifying the gradient or spatial variation of the electric field.

4.1. Test Specimens

A pristine and defective CFRTP laminate were manufactured by stacking twenty unidirectional CF/PPS plies in a [(90°/0°/45°$_2$/90°$_2$/-45°$_2$/0°/90°)]$_s$ lay-up. The CFRTP laminate without defect was employed as a reference point to assess the response of the PM and H sensors. These responses were then compared with the reception signals from sensors in the presence of a defect. The intention behind introducing the flawed laminate, as depicted in the Fig. 7, was to enable the evaluation of the PM and H sensors' capability to detect localized changes in electrical characteristics induced by distinct-sized PTFE tapes (Tooltec® A005 supplied by AIRTECH Europe SARL) positioned on varying plies throughout the laminate's thickness.

Subsequently, the sensitivity of both sensor types to defects was assessed in a configuration closer to the final application. Specifically, the sensors were attached to pristine (Fig. 8.a) and defective (Fig. 8.b) CF/PPS lap joints. In the defective joint, a single size (8×8 mm) of adhesive tape was positioned within the bonding region to artificially replicate the lack of weld defect. The welded joints were manufactured using commercially sourced rather than being subject to in-house manufacturing processes. This deliberate strategy was intended to minimize the presence of pre-existing defects in the material, which could potentially impact the analysis and lead to erroneous conclusions. These specimens were employed to examine how the proximity of joint edges influences eddy current distortion and, subsequently, the impact on the damage-detection sensitivity of the PM and H sensors.

4.2. Fabrication

Fig. 9 shows the primary steps employed in the manufacturing of defective CFRTP laminate. (a) Prepreg sheets were stacked to align fiber orientations according to the designed layup. PTFE adhesive square tapes, varying in dimensions (15×15, 10×10, 8×8, 5×5, 2×2 mm), were positioned at distinct plies as depicted in Fig. 7. (b) The consolidation process was conducted within an autoclave, following pressure and temperature profiles in agreement with the specifications provided in the manufacturer's prepreg technical sheet. (c) CFRP laminate with embedded artificial defect was then obtained.

To produce the welded specimen, a commercial induction welding machine (Bielec S.L.) was utilized. This machine includes a multifunctional controller responsible for operating a solid-state frequency generator. Additionally, an infrared pyrometer was integrated into the setup to measure the temperature on the composite surface in closest proximity to the induction coil. Energy transmission to the CFRP laminates was executed through a solenoid inductor as shown in Fig. 10.a, which was positioned by an industrial robot (KUKA). To prevent any thermal damage to the upper surface of the workpiece (depicted in Fig. 10.a), sufficient air cooling was employed. Furthermore, the consolidation process was completed using an adjustable pressure application system featuring two rollers. Fig. 10.b shows the PTFE adhesive tapes positioned in the bond line before the welding operation.
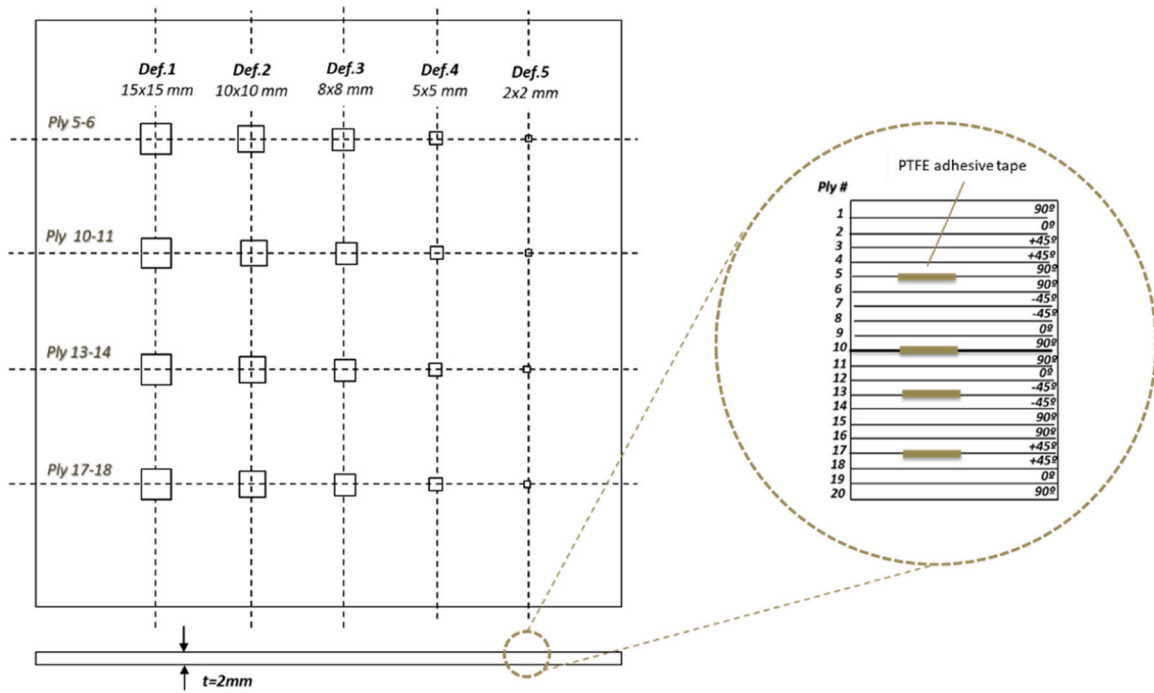
Fig. 7. Schematic drawing of CF/PPS laminates fabricated by embedding PTFE adhesive tapes of different sizes and (b) placed at different plies along the thickness in order to generate in a controlled manner a local variation of the electromagnetic characteristics of the material.
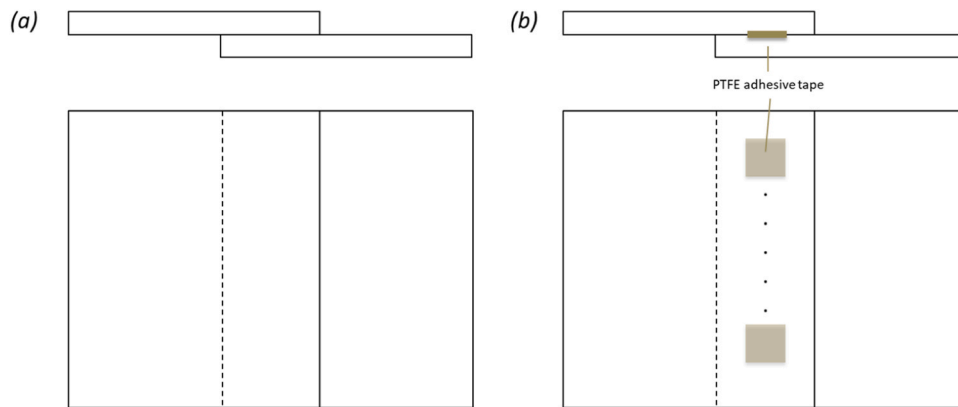

Fig. 8. Schematic drawing of (a) pristine and (b) defective CF/PPS welded lap-joint.

Fig. 11 illustrates the meticulous photolithography process employed for the fabrication of sensors utilized in the present study. The process begins with the lamination of a substrate, comprising FR4 epoxy glass fiber, with layers of copper and photoresist (Fig. 11 (a)). Subsequently, the photoresist-coated substrate undergoes exposure to ultraviolet (UV) light using a mask that replicates the desired geometry of the emission loop (Fig. 11 (b)). Following exposure, a development process selectively removes the exposed photoresist areas, revealing the emission loop pattern on the substrate (Fig. 11 (c)). The exposed copper areas, not protected by the developed photoresist, are then etched away, resulting in the formation of the emission loop pattern (Fig. 11 (d)). Subsequent stripping removes the remaining photoresist, leaving behind the finalized emission loop on the substrate (Fig. 11 (e)). After the substrate is flipped over, the same steps are repeated (Fig. 11 from (f) to (l)) to fabricate the reception loop in the case of the PM sensor or the sensing elements in the case of the H sensor.

Subsequent to fabrication, the sensors were attached to the components using an adhesive that ensured strong attachment and facilitated easy repositioning if required. To ensure accurate positioning of the sensors relative to defects within the manufactured components, a meticulous approach was adopted. Specifically, prior to sensor application, the defects' precise locations on the components were delineated using a marker, as illustrated in Fig. 9(c). This methodical marking process enabled precise alignment between the sensors and defects, ensuring accurate detection and characterization of introduced anomalies.

4.3. Test setup

The PM sensor and H sensor were positioned in the specimens as indicated in the Fig. 12(c) and (d) in order to evaluate changes in the electrical properties of the inspected materials induced by defect presence. The frequency sweep was conducted using the frequency response analyzer built –in the Moku Pro platform, which generated a sinusoidal signal with a frequency varying from 0.1 and 7 MHz and an output voltage of 10 Vppk. This signal was used to feed the emission loop of both sensors connected via coaxial cables, as shown in Fig. 12(a) and (b) for PM and H sensors, respectively. The signal of the sensing elements for
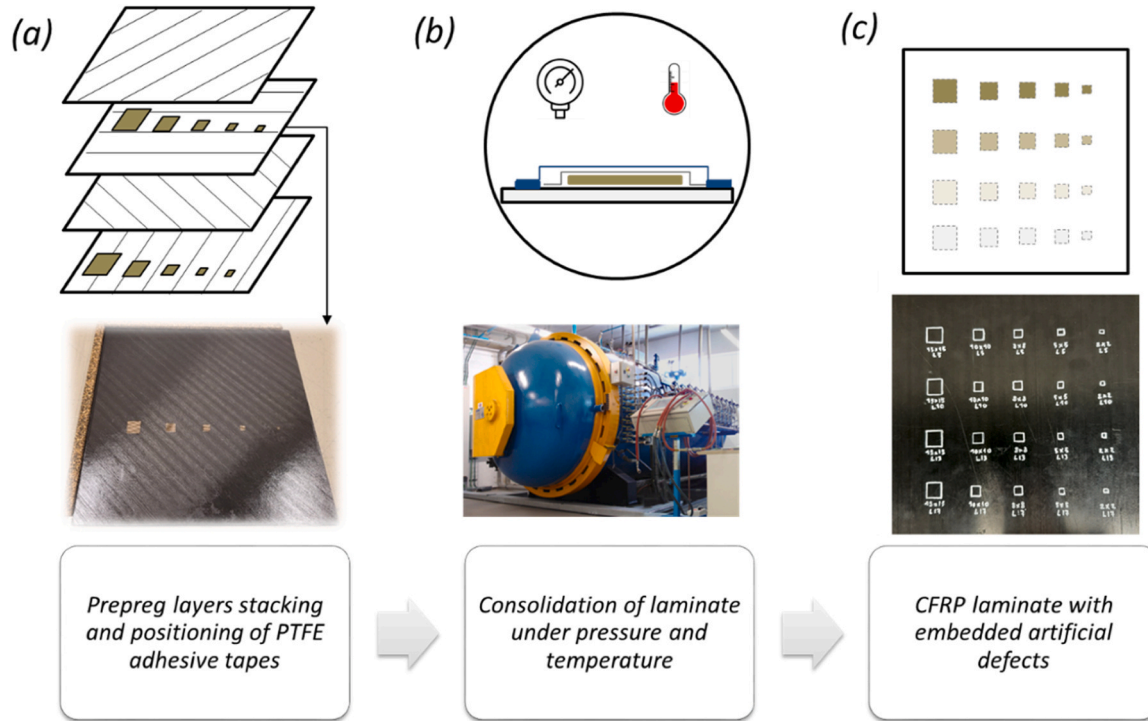
Fig. 9. Main steps of manufacturing process to obtain CFRP laminate with embedded artificial defects.
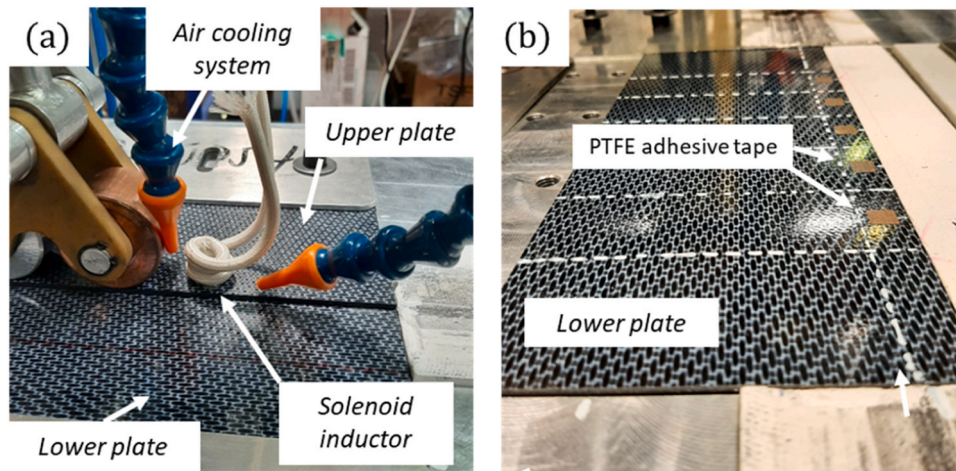

Fig. 10. (a) Relevant components of Induction welding system. (b) PTFE adhesive tapes placed in the joint line for obtaining defective welds in a fully controlled way.

each sensor was collected by the Moku Pro inputs and displayed for each frequency point. For the PM sensor, reception loop terminals were directly connected to the instrument's input. In the case of H sensors, two coaxial cables were employed. Each cable's positive polarity was connected to one of the sensing electrodes, while the negative polarities of both cables were interconnected to accurately measure the potential difference between the two sensing electrodes. To ensure the stability and reliability of our measurements, each frequency sweep process was meticulously repeated 10 times. This repetition allowed us to observe and analyze the consistency of the sensor signals across multiple iterations, thereby verifying the absence of significant drift or fluctuations that could compromise the accuracy of our data. The choice of conducting 10 repetitions was based on statistical considerations to achieve a robust assessment of signal stability and to detect any subtle variations or anomalies that might occur over time due to electronics or potential

material heating associated with eddy currents. No relevant variations were detected in any of the repeated measurements (below 2 %), confirming the accuracy of the collected data.

5. Results and discussion

5.1. Sensor's response on air and on sound joint

In the following discussion, we define the "on air response" of a sensor as the voltage exhibited by its sensing elements in response to variations in excitation frequency and in the absence of the material to be inspected. The evaluation of the on air response holds paramount significance, as it serves as the keystone upon which the subsequent interpretation of signal alterations arising from the presence of an inspected material and any potential damage relies. Fig. 13 (a) and (b)
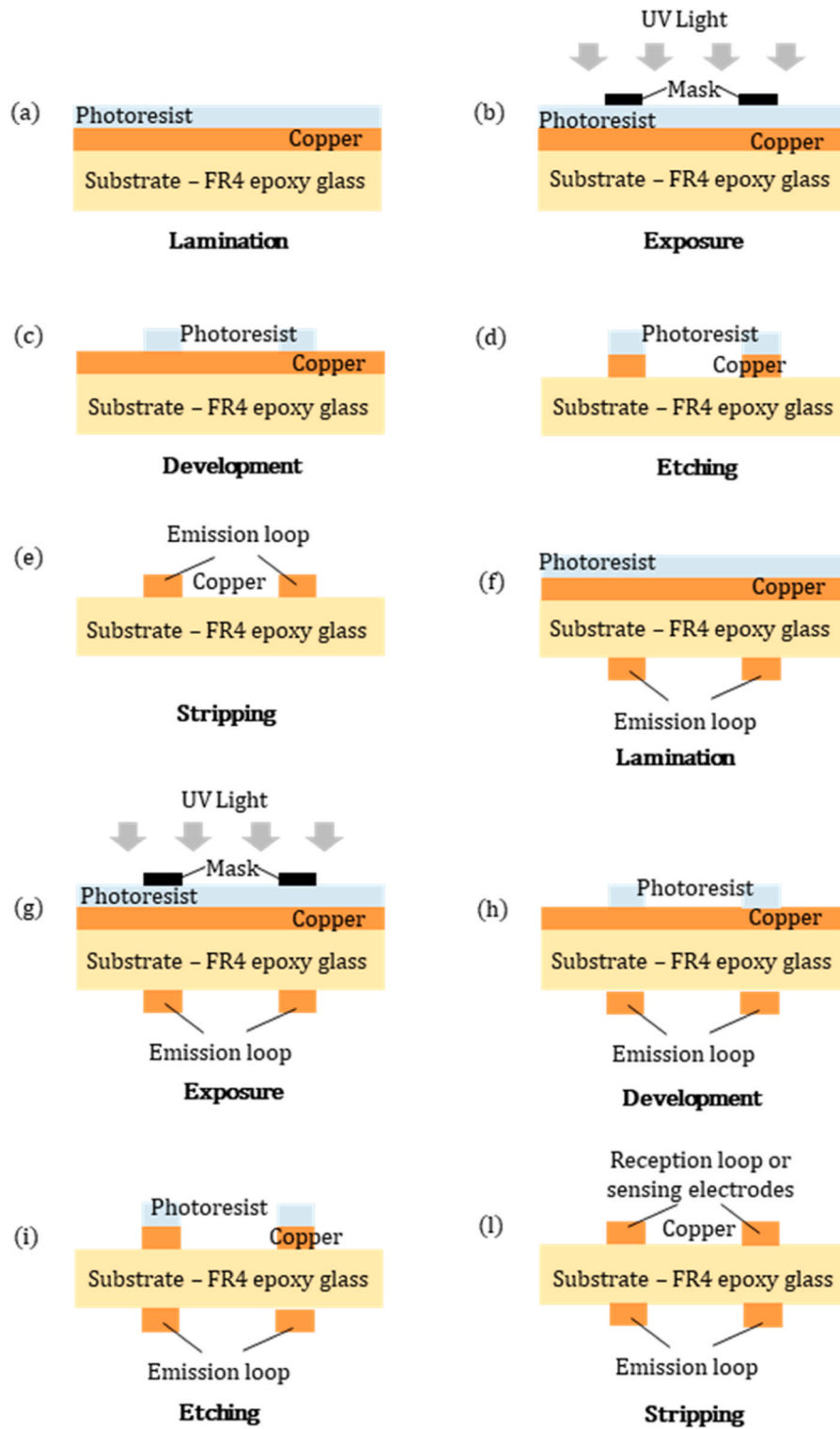
Fig. 11. Main steps of photolithography process for PM and H sensors fabrication.

show, respectively, the on air response of the PM and H sensor. Specifically, for the PM sensor, the voltage across the reception loop is measured, while for the H sensor, the voltage across the electrodes is considered. Considering firstly the on air response of the PM sensor, for frequencies below 4 MHz a direct proportionality exists between the induced voltage in the reception coil and the exciting frequency as is clearly evident by looking at the dotted line. This tendency finds a clear explanation by considering Faraday's law and in particular the equation

[22]: in this frequency range we can consider an ideal inductance behaviour of the sensor components, and the mutual inductance between emission and reception loop M_{10} could be considered constant. In fact, M_{10} is only function of the geometrical characteristics of the emission and reception loop and their relative distance. As the frequency increases, skin effect and stray capacitance begin to become present in the emission loop, and the on air response deviates from the linear trend from just over 4 MHz as shown in Fig. 13 (a). Examining the response of
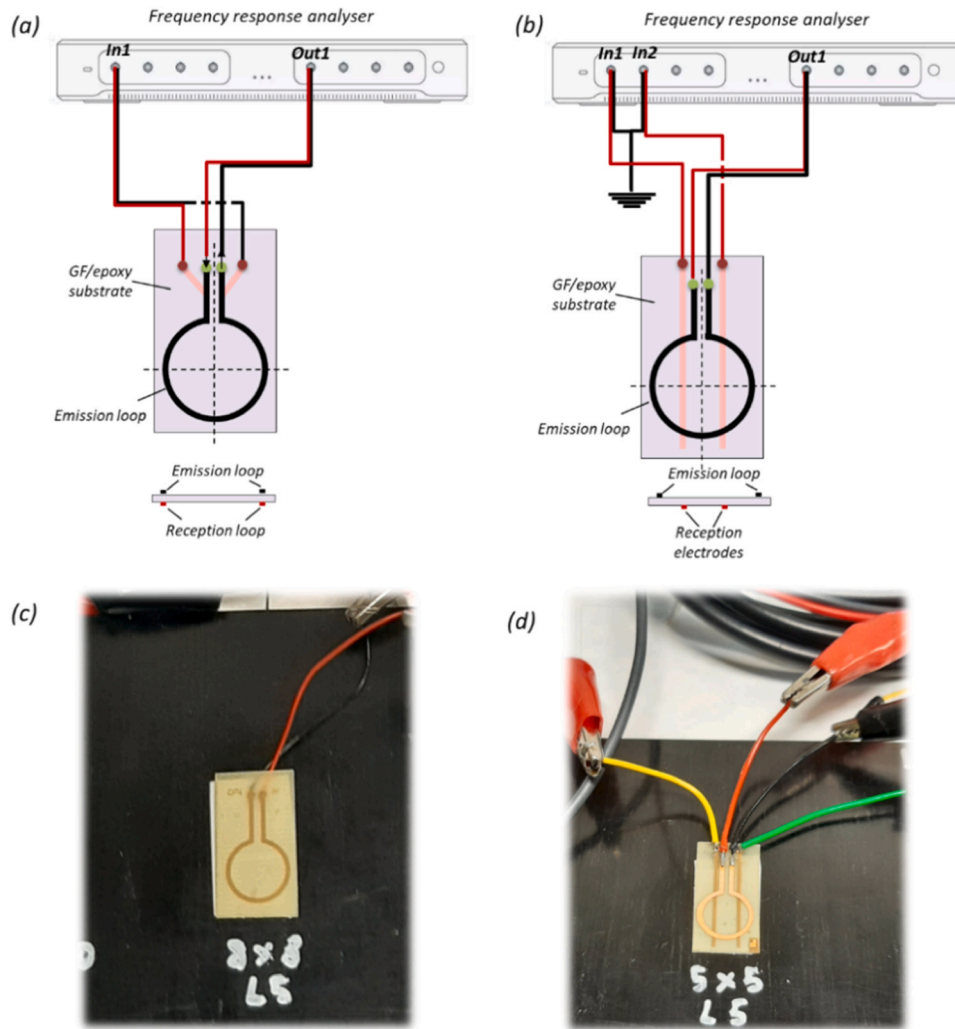
Fig. 12. Damage sensing set-up for (a) PM and (b) HB sensor. Photos of (c) PM and (d) HB sensor attached on the defective plate.
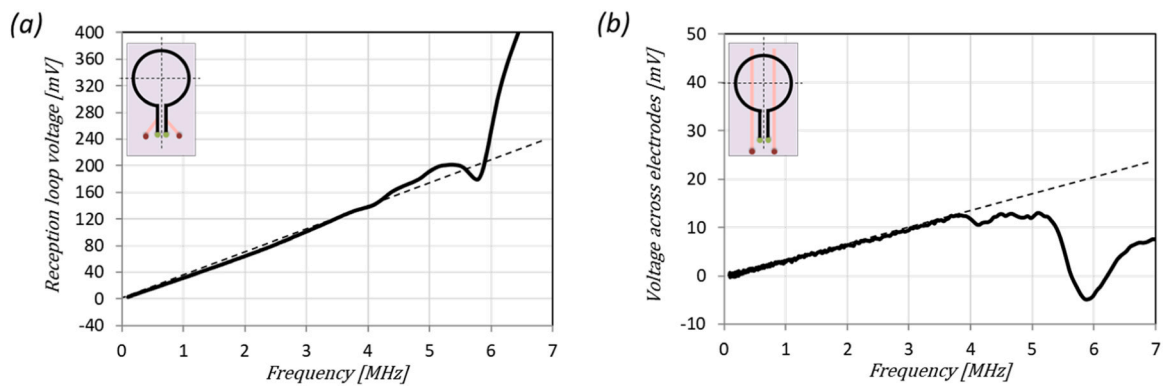

Fig. 13. On air response of (a) purely magnetic (PM) and (b) hybrid (H) sensor.

the H sensor in Fig. 13 (b), a noteworthy linear relationship is evident between the measured electric field and the excitation frequency up to approximately 4 MHz. However, it's important to note that the voltage values in this case are noticeably lower compared to those achieved with the PM sensor.

Considering instead the interaction of the sensors with an inspected material, Fig. 14 shows the change in sensor responses as soon as they are attached in a CFRTP laminate. V and V_0 represent respectively the

induced voltage in the presence of the CFRTP laminate and the on air response. V/V_0 ratio expresses the level of electromagnetic response of the material in the considered frequency range. Such curves serve a crucial purpose in highlighting specific frequency ranges where even minor local alterations in the material's electrical properties, such as defects, play a substantial change in the electromagnetic response. A notable pattern emerges for the PM sensor as shown in Fig. 14: up to the 5.5 MHz threshold, there is minimal discernible change in sensor
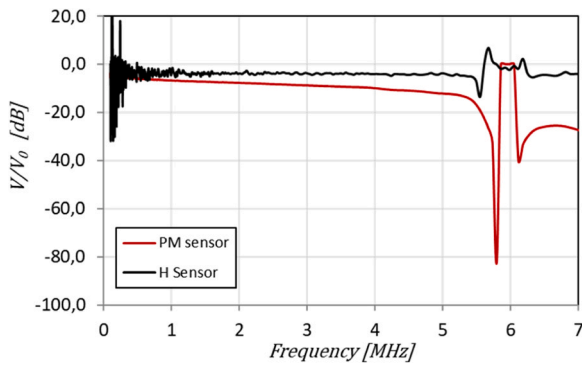
Fig. 14. Level of electromagnetic response of a pristine CF/PPS laminate when inspected by PM and H sensor.

response when transitioning from an absence of laminated CFRTP to its presence. The reception loop voltage undergoes only a slight, linear modification with frequencies in this range. However, as we approach the frequency range around 6 MHz, a noteworthy shift occurs with a significant increase in V/V_0 ratio values. Within this range, two distinct peaks become discernible. Variations in electromagnetic properties associated with the presence of defects could produce more pronounced sensor response variations in these frequency ranges, and consequently it is in these areas that greater damage sensitivity is expected. In addition, the negative values expressed in dB of the curve associated with the PM sensor emphasize that as the sensor approaches the material, a reduction in the reception loop voltage with respect to the value associated with the on-air response condition is observed. This phenomenon finds a clear explanation considering that the eddy currents induced in the material generate a magnetic field opposite to that one that generated it. Consequently, the concatenated flux is lower leading to a lower induced voltage in the reception loop in accordance with Faraday's law (see equation [12]).

On the other hand, with regard to the variation of V/V_0 by engaging the H sensor, it can be seen in Fig. 14 that the measured voltage is generally lower than in the PM sensor case throughout the measured frequency rank. The response of the H sensor in switching from the no condition to the presence of the laminated CFRTP is characterized by considerable noise for frequencies below 1 MHz and almost no relevant signal change up to about 5.5 MHz. From here on there is a greater signal variation as for the PM sensor case although of lesser magnitude. From this first comparison, it is possible to observe that the level of electromagnetic response of a non-perfectly conducting material such as a pristine CFRTP laminate is more strongly detected when measurements of the magnetic field (PM sensor) are made than when measurements of the electric field (H sensor) are performed. However, in both

cases, the frequency range between 5.5 MHz and 6.5 MHz exhibits the highest sensitivity, wherein minor local changes in the electrical properties of the material, such as defects, can significantly alter the electromagnetic response of the composite.

5.2. Sensors responses on defective laminate

Fig. 15 and Fig. 16 illustrate the detection capability of the sensors in identify anomalies that induce alterations in the electromagnetic characteristics of the material, as defect size and position vary along the thickness of the flawed CFRTP laminated composite. In light of the preceding discourse, we selected two excitation frequencies for analysis: one localized in the region where limited sensitivity to defect detection is expected, and the other proximal to the area characterized by higher sensitivity to the presence of damage.

Fig. 15 (a) shows how for the lower frequency of 3 MHz, a slight increase in reception loop voltage is observed as the defect size increases. This trend is accentuated by using an excitation frequency near the area of highest damage sensitivity (5.3 MHz). The reason behind the amplification of reception loop voltage with an augmentation in defect size is found in the localized alteration of the electrical properties of CFRTP laminate. As previously exposed, CFRTP laminate comprises a conductive constituent (carbon fiber) and a dielectric constituent (the polymer matrix). With the increase of defect size, the dielectric component increases locally, leading to a concomitant reduction in the intensity of induced currents. The lower entity of induced currents, in turn, give rise to a lower magnetic field opposing that generated by the excitation loop. Consequently, as the defect size increases, the magnetic flux lines concatenated to the reception loop exhibit greater intensity, leading to a corresponding increase in induced voltage.

With regard to the H sensors, it can be observed that there is no clear trend in the voltage of the sensing element as in the case of the PM sensor. The signal variations for this type of sensor are a function of both local electrical conductivity and dielectric permittivity values as expressed by equation [10]. These two local variations in electrical properties may either align harmoniously with or diverge from the overall contribution to the electric field making more difficult to obtain a clear trend as the defect size increases. Observing Fig. 15 (b), an increasing trend in voltage across the electrodes can be observed for an excitation frequency of 5.7 MHz, starting with a defect area of 25 mm^2. Assuming that the major contribution to the electric field is the field resulting from the polarization phenomenon, this trend can be explained by a local increase in dielectric permittivity as the size of the PTFE adhesive square tapes embedded in the laminate increases. In the case of the smaller defect (with an area of 4 mm^2), the increased voltage observed across the electrodes can be attributed to a greater contribution of the electric field component originating from free charges. As explained previously, the electric field is a combination of contributions
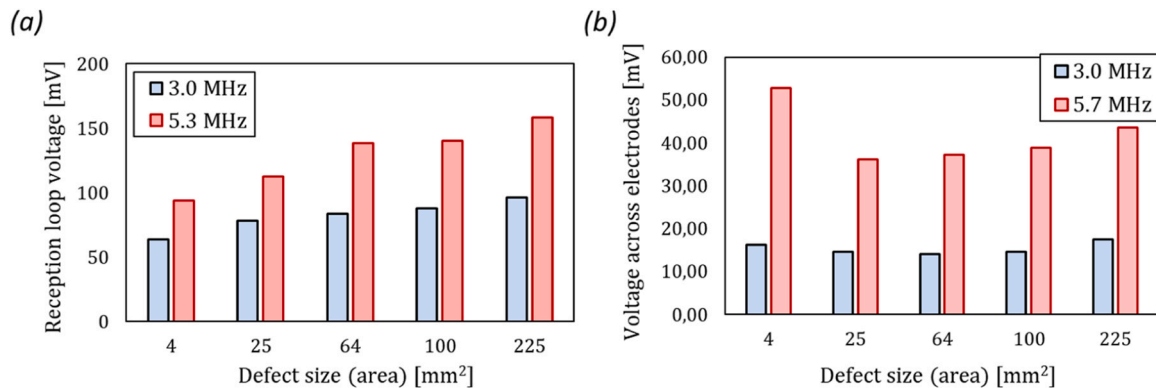

Fig. 15. Variation of the (a) PM and (b) H sensor response for different defect size defects in CFRTP laminate (area of the PTFE adhesive square tapes located between ply 5 and 6).
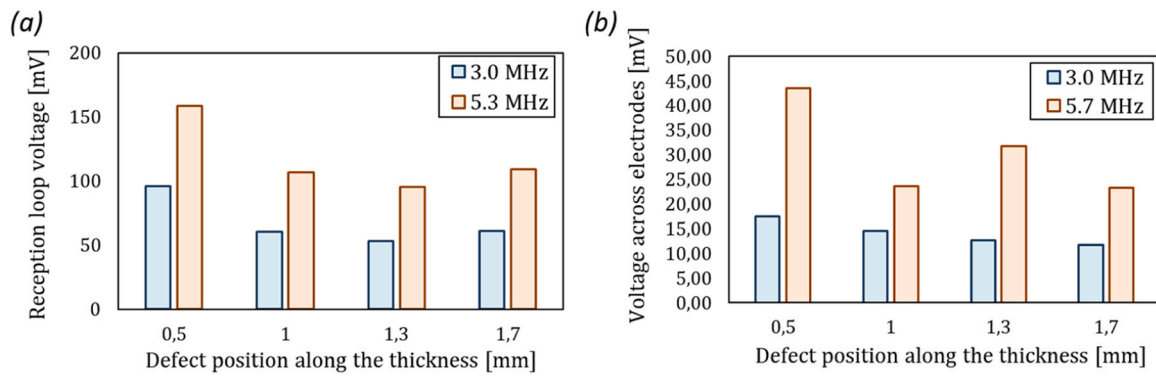
Fig. 16. Variation of the (a) PM and (b) H sensor response for different location of the defects in CFRTP laminate (15×15 mm PTFE adhesive square tapes located at different plies along the thickness).

from free charges and polarization phenomena. For larger dielectric components, polarization phenomena dominate. However, with the smaller PTFE adhesive square, the conduction phenomenon associated with free charges in the carbon fiber reinforcement also becomes significant. The overall increase in the measured electric field values could therefore be associated to the alignment of both contributions, leading to the observed increase in voltage.

At an excitation frequency of 3 MHz, there is a lack of discernible voltage fluctuations when defect size is changed, as was expected since the frequency is in an area considered to have low damage sensitivity.

With regard to the variation of the signal as the position of the defect changes, Fig. 16 shows how the response of the two sensors varies by varying the position of the PTFE adhesive square tape of a given size (15×15 mm) along the thickness. In the case of the PM sensor, illustrated in Fig. 15 (a), it is noteworthy that, across both examined frequencies, a consistent reduction in reception loop voltage is observed as the defect is positioned deeper within the material's thickness. This decrease in voltage remains the trend until the PTFE adhesive square tape is located at the furthest point, situated at a distance of 1.7 mm from the surface where the sensor is mounted, where only a marginal increase in reception loop voltage is detected.

This trend can be explained by considering that when a sinusoidal time-varying magnetic field is generated by the exciting loop, the induced current density decreases exponentially through the thickness. As the PTFE adhesive square is closer to the surface, the induced currents having higher intensity are notably influenced. In fact, their trajectory is altered, and their intensity diminishes due to localized reductions in electrical conductivity. Consequently, the magnetic field that opposes the originating field is lower, leading to a higher induced voltage in the reception loop. Conversely, when the PTFE adhesive square is positioned farther from the surface, the impact on the stronger induced currents is less pronounced, resulting in a greater reduction in the magnetic flux linked to the reception loop. Considering Fig. 16 (b) relative to H sensor, when subjected to an excitation frequency of 3 MHz, a slight decline in voltage across the electrodes becomes apparent. This phenomenon is explicable by the proximity of the PTFE adhesive square to the material's surface, which results in a localized augmentation of dielectric permittivity and, consequently, an amplification of the measured electric field. In contrast, when the frequency is set at 5.7 MHz, the positioning of the artificially induced defect throughout the material's thickness does not reveal a distinct and consistent pattern. In this scenario, it is hypothesized that voltage fluctuations across the electrodes may arise from potential variations in the distribution of free charges along the carbon fibers, coupled with potential alignment changes of electric dipoles within both the polymer matrix and the PTFE adhesive square tape. For this specific excitation frequency, the contributions of these elements to the total electric field may either align harmoniously or oppose each other, contingent on the

positional changes of the PTFE adhesive square.

5.3. Sensors responses on welded lap joint

With the aim of evaluating the performance of the two sensors for SHM of thermoplastic welded joints, Fig. 17 and Fig. 18 show, respectively, the variation of the PM and H sensor response over the frequency range considered in the case of pristine and defective welded joints. In this respect, it is useful to introduce the following parameter in order to evaluate changes of a reference signal corresponding to the sound structure when a damage induces a local variation of the electromagnetic properties of the material:

$$\Delta V = 20 \quad \log_{10} \left[\frac{V_{defect}}{V_{sound}} \right]$$

where ΔV is called "damage sensitivity" and V_{defect} and V_{sound} are respectively the induced voltage of the sensing component of the sensor in the presence and absence of a defect. Looking at Fig. 17 (a), it can be seen that the PM sensor response has a similar trend to that seen in the CFRTP laminate inspection, with a linear trend up to about 5 MHz and then a subsequent signal variation as skin effect and parasitic capacitance occurs. The frequency range between 5 and 6 MHz reveals the most significant deviations in reception loop voltage between pristine and defective joint conditions. This higher damage sensitivity range is most evident by showing the variation of the ΔV parameter as shown in Fig. 17 (b) where it is possible to identify a sensitivity peak near the 6 MHz excitation frequency. With regard to the response of the H sensor, again no relevant signal variations from the pristine baseline are observed for frequencies below 5 MHz, as shown in Fig. 18. For frequencies between 5 and 7 MHz, on the other hand, damage sensitivity peaks can also be identified with values exceeding those encountered for the PM sensor.

6. Conclusion

In this research, a sinusoidal time-varying magnetic field was generated using a single loop coil, referred to as the emission loop, in close proximity to the materials under inspection. Two distinct measurement methodologies were employed to investigate the interaction between alterations in electrical properties resulting from damage in CFRTP and the generated magnetic field. The first method, referred to as purely magnetic method, involved measuring the magnetic field using a sensing loop positioned between the emission loop and the inspected material (PM sensor). The second approach is a hybrid method, focused on measuring changes in the electric field caused by defects using a pair of sensing electrodes (H sensors). The effectiveness of these electromagnetic field techniques was evaluated by inspecting a laminate deliberately subjected to induced defects, replicating local variations in
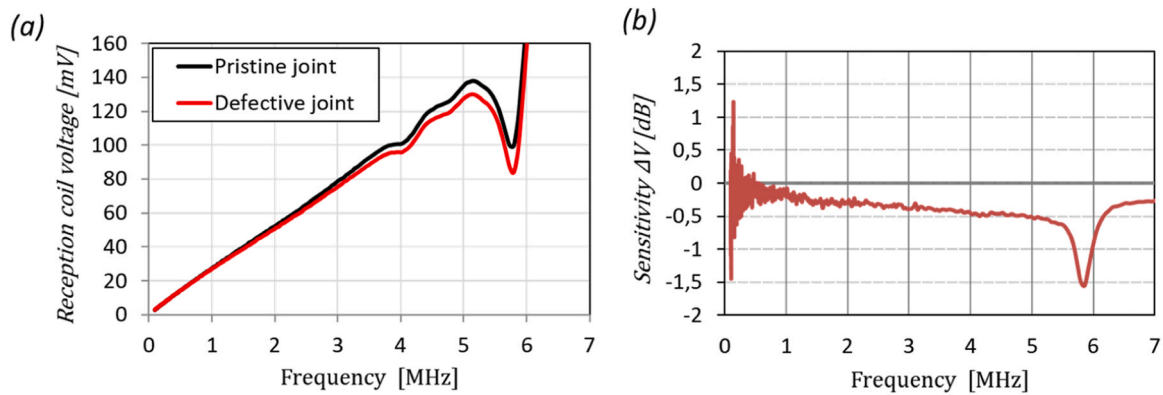
Fig. 17. (a) PM sensor response during pristine and defective welded joint inspection and (b) spectrum of damage sensitivity.
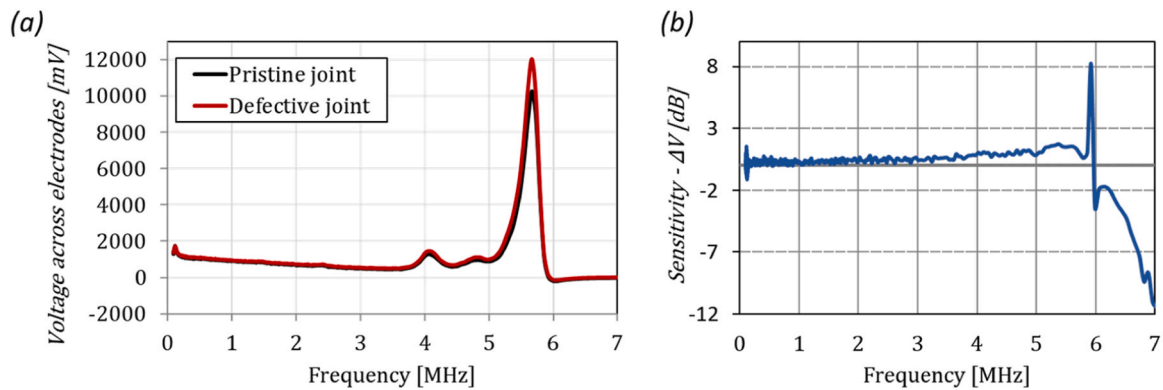

Fig. 18. (a) H sensor response during pristine and defective welded joint inspection and (b) spectrum of damage sensitivity.

electrical properties. These defects were created by placing a square PTFE adhesive tape on a specific ply during the stacking process. The PTFE adhesive tapes, of various sizes and localized at different ply positions along the thickness, locally affected both the dielectric permittivity and electrical conductivity of the CFRTP laminate. By comparing the response of the sensors in the absence and presence of the laminated CFRTP in a range of excitation frequencies between 0.1 and 7 MHz, it is possible to identify areas where greater sensitivity to defect-induced changes in electromagnetic properties would be expected from 5 MHz onward. Particularly, when measuring the magnetic field using the PM sensor, there is an increasing variation in the reception loop voltage as the size of the embedded PFTE adhesive square increases. In contrast, the magnitude of the PM sensor response decreases as the PTFE adhesive square moves further away from it along the thickness. These results underscore that measuring the magnetized field using the PM sensor is a potentially effective SHM method for monitoring defect propagation in CFRTP laminates and for locating defects in proximity to the sensor installation zone. When assessing changes in the electric field using the H sensor as the size and position of artificially created defects in the laminate changed, it did not exhibit clear trends as observed in the case of the PM sensor. However, when assessing damage sensitivity in defective thermoplastic welded joints, the H sensor demonstrated signal variations from the baseline (pristine joint) at approximately 8 dB, markedly higher than those observed with the PM sensor (at an absolute value of 1.5 dB), using an excitation frequency of 5.9 MHz. In conclusion, employing magnetic and electric field measurements to detect changes in damage-induced electrical properties constitutes a potentially effective method for structural health monitoring in thermoplastic welded CFRTP joints. The purely magnetic method demonstrates significant potential for quantifying and localizing damage-inducing changes in electromagnetic proprieties, while the hybrid method stands out for its notable damage sensitivity values.

In conclusion, our study highlights the promising potential of the investigated methods in SHM field. While our initial focus on controlled variations of electromagnetic properties provided valuable insights into their effectiveness, future research endeavors will include validation with real defects to further enhance their applicability and ensure a comprehensive evaluation under practical scenarios. An additional practical scenario worthy of investigation involves assessing how the presence of pre-existing defects in the laminates may influence the sensor's assessment of weld integrity—a noteworthy aspect poised for future research endeavors.

CRediT authorship contribution statement

Karina Carla Nuñez Carrero: Writing – review & editing, Validation, Supervision, Methodology, Funding acquisition, Formal analysis. **Esteban Cañibano:** Validation, Software, Formal analysis. **Juan Carlos Merino Senovilla:** Software, Resources, Funding acquisition, Formal analysis. **Mattia Mazzeschi:** Writing – original draft, Validation, Methodology, Investigation, Formal analysis, Data curation, Conceptualization. **Saman Farhangdoust:** Writing – review & editing, Visualization, Validation, Methodology, Data curation.

Declaration of Competing Interest

The authors declare that they have no known competing financial interests or personal relationships that could have appeared to influence the work reported in this paper.

Data availability

The data that has been used is confidential.

Acknowledgment

References

[1] M. Favaloro, A comparison of the environmental attributes of thermoplastic vs. thermoset composites, Int. SAMPE Tech. Conf. (2009) 1–6.

[2] Market Research Future, "Thermoplastic Composite Market Research Report Information," 2023. [Online]. Available: ⟨https://www.marketresearchfuture.com/reports/thermoplastic-composites-market-4244⟩.

[3] J.P. Reis, M. de Moura, S. Samborski, Thermoplastic composites and their promising applications in joining and repair composites structures: a review, Mater. (Basel) vol. 13 (24) (2020) 1–33, https://doi.org/10.3390/ma13245832.

[4] S.K. Bhudolia, G. Gohel, K.F. Leong, A. Islam, Advances in ultrasonicwelding of thermoplastic composites: a review, Mater. (Basel) vol. 13 (6) (2020), https://doi.org/10.3390/ma13061284.

[5] Y. Wang, Z. Rao, S. Liao, F. Wang, Ultrasonic welding of fiber reinforced thermoplastic composites: Current understanding and challenges, in: Composites Part A: Applied Science and Manufacturing, vol. 149, Elsevier Ltd, 2021, https://doi.org/10.1016/j.compositesa.2021.106578.

[6] D. Brassard, M. Dubé, J.R. Tavares, Resistance welding of thermoplastic composites with a nanocomposite heating element, Compos. Part B Eng. vol. 165 (2019) 779–784, https://doi.org/10.1016/j.compositesb.2019.02.038.

[7] X. Xiong, et al., Resistance welding technology of fiber reinforced polymer composites: A review, in: Journal of Adhesion Science and Technology, vol. 35, Taylor and Francis Ltd, 2021, pp. 1593–1619, https://doi.org/10.1080/01694243.2020.1856514.

[8] T.J. Ahmed, D. Stavrov, H.E.N. Bersee, A. Beukers, Induction welding of thermoplastic composites-an overview, Compos. Part A Appl. Sci. Manuf. vol. 37 (10) (2006) 1638–1651, https://doi.org/10.1016/j.compositesa.2005.10.009.

[9] T. Bayerl, M. Duhovic, P. Mitschang, D. Bhattacharyya, The heating of polymer composites by electromagnetic induction - A review, Compos. Part A: Appl. Sci. Manuf. vol. 57 (2014) 27–40, https://doi.org/10.1016/j.compositesa.2013.10.024.

[10] S. Becker, M. Michel, P. Mitschang, M. Duhovic, Influence of polymer matrix on the induction heating behavior of CFRPC laminates, Compos. Part B Eng. vol. 231 (2022), https://doi.org/10.1016/j.compositesb.2021.109561.

[11] L. Moser, P. Mitschang, A. Schlarb, Robot based induction welding of thermoplastic polymer composites, Int. SAMPE Symp. Exhib. vol. 52 (Jan. 2008).

[12] H. Fu, D. Bekas, Z.S. Khodaei, and M.H.F. Aliabadi, "Structural Health Monitoring for condition based maintenance of composite structures," in *SHM-NDT 2018 - International Symposium on Structural Health Monitoring and Nondestructive Testing*, 2018. [Online]. Available: ⟨http://www.ndt.net/?id=23538⟩.

[13] BINDT, "Report from the Workshop on NDT and SHM Requirements for Aerospace Composites," *Work. NDT SHM Requir. Aerosp. Compos.*, no. February, 2016, [Online]. Available: https://compositesuk.co.uk/system/files/documents/2016 BINDT Workshop on NDT and SHM Requirements for Aerospace Composites - Report FINAL.pdf.

[14] R.W. Ross, Integrated vehicle health management in aerospace structures, Elsevier, 2016, https://doi.org/10.1016/B978-0-08-100148-6.00001-9.

[15] M. Mitra, S. Gopalakrishnan, Guided wave based structural health monitoring: a review, Smart Mater. Struct. vol. 25 (5) (2016), https://doi.org/10.1088/0964-1726/25/5/053001.

[16] W. Ostachowicz, P. Kudela, M. Krawczuk, and A. Zak, Guided Waves in Structures for SHM The Time-Domain Spectral Element Method of Fluid Flow Machinery. 2011. [Online]. Available: ⟨www.wiley.com⟩.

[17] P. Jiao, K.J.I. Egbe, Y. Xie, A.M. Nazar, A.H. Alavi, Piezoelectric sensing techniques in structural health monitoring: a state-of-the-art review, Sens. (Switz.) vol. 20 (13) (2020) 1–21, https://doi.org/10.3390/s20133730.

[18] M. Saeedifar, D. Zarouchas, Damage characterization of laminated composites using acoustic emission: a review, Compos. Part B Eng. vol. 195 (January) (2020) 108039, https://doi.org/10.1016/j.compositesb.2020.108039.

[19] C. Muir, et al., Damage mechanism identification in composites via machine learning and acoustic emission, npj Comput. Mater. vol. 7 (1) (2021) 1–15, https://doi.org/10.1038/s41524-021-00565-x.

[20] M. Sadri, D. Younesian, Vibroacoustic analysis of a sandwich panel coupled with an enclosure cavity, Compos. Struct. vol. 146 (2016) 159–175, https://doi.org/10.1016/j.compstruct.2016.03.024.

[21] J.K. Sahota, N. Gupta, D. Dhawan, Fiber bragg grating sensors for monitoring of physical parameters: a comprehensive review, Opt. Eng. vol. 59 (06) (2020) 1, https://doi.org/10.1117/1.oe.59.6.060901.

[22] K. Bednarska, et al., Hybrid fiber optic sensor systems in structural health monitoring in aircraft structures, Mater. (Basel) vol. 13 (10) (2020) 1–17, https://doi.org/10.3390/ma13102249.

[23] L. Yu, Z. Tian, Phased array techniques for damage detection in aerospace structures, Struct. Heal. Monit. Aerosp. Struct. (2016) 285–306, https://doi.org/10.1016/B978-0-08-100148-6.00010-X.

[24] S. Farhangdoust, A. Mehrabi, Health monitoring of closure joints in accelerated bridge construction: a review of non-destructive testing application, J. Adv. Concr. Technol. vol. 17 (Jul. 2019) 381–404, https://doi.org/10.3151/jact.17.381.

[25] D. Goyal, B.S. Pabla, The vibration monitoring methods and signal processing techniques for structural health monitoring: a review, Arch. Comput. Methods Eng. vol. 23 (4) (2016) 585–594, https://doi.org/10.1007/s11831-015-9145-0.

[26] C.P. Fritzen, Vibration-based techniques for structural health monitoring, Struct. Heal. Monit. (2010) 45–224, https://doi.org/10.1002/9780470612071.ch2.

[27] H. Hasni, P. Jiao, A.H. Alavi, N. Lajnef, S.F. Masri, Structural health monitoring of steel frames using a network of self-powered strain and acceleration sensors: a numerical study, " *Autom. Constr.* vol. 85 (2018) 344–357, https://doi.org/10.1016/j.autcon.2017.10.022.

[28] W.S. Na, J. Baek, A review of the piezoelectric electromechanical impedance based structural health monitoring technique for engineering structures, Sens. (Switz.) vol. 18 (5) (2018), https://doi.org/10.3390/s18051307.

[29] T.N. Tallman, D.J. Smyl, Structural health and condition monitoring via electrical impedance tomography in self-sensing materials: a review, Smart Mater. Struct. vol. 29 (12) (2020), https://doi.org/10.1088/1361-665X/abb352.

[30] L. Selvakumaran, Q. Long, S. Prudhomme, G. Lubineau, On the detectability of transverse cracks in laminated composites using electrical potential change measurements, Compos. Struct. vol. 121 (2015) 237–246, https://doi.org/10.1016/j.compstruct.2014.11.008.

[31] M. Mazzeschi, K.C. Nuñez, E. Cañibano, J.C. Merino, Monitoring of thermoplastic induction welding defects. Use of electromagnetic properties as a predictive tool, Struct. Heal. Monit. vol. 0 (2) (2022) 1–15, https://doi.org/10.1177/14759217221111979.

[32] S.C. Olisa, M.A. Khan, A. Starr, Review of current guided wave ultrasonic testing (GWUT) limitations and future directions, Sens. (Switz.) vol. 21 (3) (2021) 1–28, https://doi.org/10.3390/s21030811.

[33] J. Moll, C. Kexel, S. Pötzsch, M. Rennoch, A.S. Herrmann, Temperature affected guided wave propagation in a composite plate complementing the Open Guided Waves Platform, Sci. Data vol. 6 (1) (2019) 1–9, https://doi.org/10.1038/s41597-019-0208-1.

[34] A. Dhutti, T.H. Gan, W. Balachandran, J. Kanfoud, High temperature performance of ultrasonic guided wave system for structural health monitoring of pipeline, Proc. 7th Asia-Pac. Work. Struct. Heal. Monit. APWSHM 2018 (2018) 308–316.

[35] J. Vetterlein, H. Klümper-Westkamp, T. Hirsch, and P. Mayr, "Eddy Current Testing at High Temperatures for Controlling Heat Treatment Processes," in *International Symposium (NDT-CE 2003)*, 2003.

[36] H. Wang, B. Ju, W. Li, Z. Feng, Ultrastable eddy current displacement sensor working in harsh temperature environments with comprehensive self-temperature compensation, Sens. Actuators, A Phys. vol. 211 (2014) 98–104, https://doi.org/10.1016/j.sna.2014.03.008.

[37] H. Wang, Z. Feng, Ultrastable and highly sensitive eddy current displacement sensor using self-temperature compensation, Sens. Actuators, A Phys. vol. 203 (2013) 362–368, https://doi.org/10.1016/j.sna.2013.09.016.

[38] Y. Zheng, J. Wu, and Y. Yang, "Temperature compensation of eddy current sensor based on temperature-voltage model," *Proc. World Congr. Intell. Control Autom.* , vol. 2016-Septe, pp. 438–441, 2016, doi: 10.1109/WCICA.2016.7578616.

[39] B. Lei, P. Yi, Y. Li, J. Xiang, A temperature drift compensation method for pulsed eddy current technology, Sens. (Switz.) vol. 18 (6) (2018), https://doi.org/10.3390/s18061952.

[40] N. Goldfine, V. Zilberstein, D. Schlicker, D. Grundy, Eddy-Current in situ Sensors for SHM, Encycl. Struct. Heal. Monit. (i) (2008) 1–14, https://doi.org/10.1002/9780470061626.shm080.

[41] Q. Liu, H. Sun, T. Wang, X. Qing, On-site health monitoring of composite bolted joint using built-in distributed eddy current sensor network, Mater. (Basel) vol. 12 (7) (2019), https://doi.org/10.3390/ma12172785.

[42] M.B. Lemistre, D.L. Balageas, Health monitoring system for composite material using electromagnetic measurement, SPIE - Int. Soc. Opt. Eng. (2002) 272–281, https://doi.org/10.1117/12.469886.

[43] M.B. Lemistre, D.L. Balageas, A hybrid electromagnetic acousto-ultrasonic method for SHM of carbon/epoxy structures, Struct. Heal. Monit. 2 (2) (2003) 153–160, https://doi.org/10.1177/1475921703002002007.

[44] M. Lemistre, Low Frequency Electromagnetic Techniques. Structural Health Monitoring, Wiley-ISTE, 2010, pp. 411–461, https://doi.org/10.1002/9780470612071.ch6.

[45] L. Zhang, et al., Fatigue damage monitoring of repaired composite wind turbine blades using high-stability buckypaper sensors, Compos. Sci. Technol. vol. 227 (2022) 109592, https://doi.org/10.1016/j.compscitech.2022.109592.

[46] L. Zhang, et al., Strain and crack growth monitoring of aluminum alloy sheet using high-sensitivity buckypaper film sensors, Sens. Actuators A Phys. vol. 363 (2023) 114697, https://doi.org/10.1016/j.sna.2023.114697.

[47] L. Zhang, et al., Damage evolution monitoring and failure level evaluation of composite bolted joints by MXene/CNTs sensors, Polym. Compos. vol. 45 (3) (2024) 2415–2426, https://doi.org/10.1002/pc.27929.

[48] L. Zhang, et al., Mechanical behavior monitoring of composite hybrid bonded-riveted joints using high-stability MXene sensors, Polym. Compos. (February) (2024) 1–13, https://doi.org/10.1002/pc.28267.

[49] P. Ochôa, I.F. Villegas, R.M. Groves, R. Benedictus, Experimental assessment of the influence of welding process parameters on Lamb wave transmission across ultrasonically welded thermoplastic composite joints, Mech. Syst. Signal Process. vol. 99 (2018) 197–218, https://doi.org/10.1016/j.ymssp.2017.06.009.

[50] P. Ochôa, I.F. Villegas, R.M. Groves, R. Benedictus, Diagnostic of manufacturing defects in ultrasonically welded thermoplastic composite joints using ultrasonic guided waves, NDT E Int vol. 107 (2019), https://doi.org/10.1016/j.ndteint.2019.102126.

[51] O.G. Kravchenko, V.S. Bonab, I. Manas-Zloczower, Spray-Assisted Microwave Welding of Thermoplastics Using Carbon Nanostructures with Enabled Health Monitoring, Polym. Eng. Sci. vol. 59 (11) (2019) 2247–2254, https://doi.org/10.1002/pen.25227.

[52] H. Frederick, W. Li, W. Sands, E. Tsai, and G. Palardy, "Multifunctional Films for Fusion Bonding and Structural Health Monitoring of Thermoplastic Composite Joints," 2020.

[53] F.D. Senghor, G. Wasselynck, H.K. Bui, S. Branchu, D. Trichet, G. Berthiau, Electrical Conductivity Tensor Modeling of Stratified Woven-Fabric Carbon Fiber Reinforced Polymer Composite Materials, IEEE Trans. Magn. vol. 53 (6) (2017), https://doi.org/10.1109/TMAG.2017.2660529.

[54] M. Javdanitehran, R. Hoffmann, J. Groh, M. Vossiek, G. Ziegmann, Effect of embedded printed circuit board (PCB) sensors on the mechanical behavior of glass fiber-reinforced polymer (GFRP) structures, Smart Mater. Struct. vol. 25 (6) (2016), https://doi.org/10.1088/0964-1726/25/6/065016.

[55] H. Song, W. Wang, Y. Zhou, and G. Zhou, "Mechanical properties of composites with embedded FBG sensors in different layer," *Proc. 2011 IEEE 5th Int. Conf. Cybern. Intell. Syst. CIS 2011*, pp. 52–56, 2011, doi: 10.1109/ICCIS.2011.6070301.

[56] B. Gao, G. Ru, Q. Ma, H. Li, Electromagnetic Multiphysics Sensing Nondestructive Testing, Vol. 1-4, First Ed, Encycl. Sens. Biosens. vol. 1–4 (November) (2022) 101–128, https://doi.org/10.1016/B978-0-12-822548-6.00115-1.

[57] A.S. Rahate, K.R. Nemade, S.A. Waghuley, Polyphenylene sulfide (PPS): State of the art and applications, Rev. Chem. Eng. vol. 29 (6) (2013) 471–489, https://doi.org/10.1515/revce-2012-0021.

[58] A. Galehdar, et al., The strong diamagnetic behaviour of unidirectional carbon fiber reinforced polymer laminates, J. Appl. Phys. vol. 112 (Dec. 2012) 11391–11392, https://doi.org/10.1063/1.4764041.

Mattia Mazzeschi received his M.D. in aerospace engineering from the University of Pisa in 2015. He is currently pursuing Ph.D. degree at the University of Valladolid and serves as a Researcher and R&D Project Engineer at CIDAUT Foundation. His research interests include structural health monitoring, non-destructive testing, AI techniques for enhanced composite damage diagnosis and thermoplastic welding.

Saman Farhangdoust is currently a Postdoctoral Scholar at the Structures and Composite Lab in the Aeronautics and Astronautics Department at Stanford University where he has led projects in multifunctional composites with an emphasis on intelligent self-sensing diagnostics for space and aircraft structures. He holds a BS in Solid Mechanics, two MS degrees in Mechanical and Civil Engineering, and a PhD in Structural Engineering.

Esteban Cañibano received his PhD. in industrial engineering from the University of Valladolid in 2006. He is currently Researcher and Manager of the department of Materials, Product and Processes at CIDAUT Foundation. His research interests include composite materials, thermoplastic welding, and mechatronics.

Juan Carlos Merino Senovilla. Professor at the Department of Condensed Matter Physics at the University of Valladolid. Director and founder of the technological research centre CIDAUT (Foundation for Transport and Energy Research and Development). More than 35 years of research and teaching in the field of composite materials.

Karina C. Núñez C. PhD in Physical Sciences, 2 MSc. in physical techniques of materials characterisation and in mechanical engineering. Fifteen years of experience managing research projects in polymeric materials. Currently, Professor in the Department of Condensed Matter Physics at the University of Valladolid. Her main research areas are composites and nanocomposites, smart materials, and sustainability.